Modeling and analysis of three-phase boost rectifier for DC fast EV charging

Jeerapong Srivichai, Kittaya Somsai, Nithiroth Pornsuwancharoen
Department of Electrical Engineering, Faculty of Industry and Technology,
Rajamangala University of Technology Isan Sakon Nakhon Campus, Sakon Nakhon, Thailand

Article Info

Article history:

Received Oct 10, 2024
Revised Jan 26, 2025
Accepted Mar 6, 2025

Keywords:

Average model
Boost rectifier
DC fast charging
Electric vehicles
Modeling and simulation
Power quality
Stability analysis

ABSTRACT

This research investigates the modeling and analysis of a three-phase boost rectifier for DC fast charging systems for electric vehicles (EVs). A mathematical model validated with MATLAB/Simulink simulations examines system behavior under various conditions. Performance analysis in the *abc* and *dq* coordinate systems reveals high consistency with theoretical calculations. The average voltage in the *dq* frame was found to be v_d was 685 V and v_q was 0 V, with a discrepancy of less than 0.1% from calculated values. However, the average current in the *dq* frame showed discrepancies due to cross-coupling effects and circuit impedance. Simulations reported i_d was 211.50 A and i_q was 93.50 A, compared to calculated values of i_d was 151.97 A and i_q was 0 V. For the output DC voltage and current, the average values were 983.05 V and 98.31 A, respectively. Three test cases were analyzed, consist of unbalanced three-phase conditions, voltage drops, and load step responses. Case 1 showed the highest total harmonic distortion (THD), Case 2 increased THD further, and Case 3 achieved the lowest THD, demonstrating improved stability under dynamic loads. These findings confirm the system's minimal deviations from theoretical predictions, enhanced voltage quality, harmonic mitigation, and improved charging efficiency for EV fast charging applications.

Corresponding Author:

Nithiroth Pornsuwancharoen
Department of Electrical Engineering, Faculty of Industry and Technology
Rajamangala University of Technology Isan Sakon Nakhon Campus
Phang Khon, Sakon Nakhon 47160, Thailand
Email: nithiroth.po@rmuti.ac.th

1. INTRODUCTION

Currently, electric vehicles (EVs) are becoming increasingly popular as a crucial solution for cutting greenhouse gas emissions and reducing reliance on fossil fuels. However, charging EVs quickly and efficiently remains a significant limitation. DC fast charging, a technology designed to minimize charging time, has been developed to meet user demands, particularly for long-distance travel at public charging stations and highway charging points. This technology operates with voltage levels ranging from 400 to 900 V, current between 100 and 200 A or higher, and power levels from 50 to 350 kW or more, depending on the characteristics of the charging station. It typically takes only 20 to 60 minutes to charge the battery to an 80% state of charge (SOC) [1], [2]. Although DC fast charging technology addresses usability needs, integrating charging systems with the power grid still faces challenges related to power system instability. Issues such as harmonics, which distort the electrical waveforms, and voltage sag, which reduces voltage levels, can affect grid stability and the efficiency of EV battery charging [3]-[8]. Additionally, the high electrical loads from charging stations may pose challenges to the power grid, particularly in energy distribution and system reliability, as noted in previous studies [9]-[11]. The mathematical modeling of three-phase AC to DC conversion, a critical component of DC fast charging systems, is essential for analyzing system behavior. Designing models that accurately reflect real system behavior, such as non-linear characteristics [12]-[14], dynamic responses [15]-[17], and the impacts of large electrical loads, is a complex and challenging task [18], [19]. This research focuses on developing a mathematical model and analyzing three-phase AC to DC conversion for fast charging systems using MATLAB/Simulink simulation [20], [21]. The aim is to accurately reflect system behavior and analyze factors affecting system stability and efficiency, such as mitigating harmonic impacts, maintaining voltage quality, and enhancing charging efficiency. This study aims to contribute to the development of stable, reliable, and efficient charging systems that can meet increasing future demands.

2. MATHEMATICAL MODEL

This section presents the mathematical model, including the average model of a three-phase boost rectifier, switching circuit, and control system. It outlines the formulations, assumptions, and analyzes the relationships between circuit parameters, system behavior, and control objectives.

2.1. Average model of three-phase boost rectifier

The boost rectifier's average model is formulated using the averaging equivalent circuit method. This approach yields a time-invariant model applicable at frequencies significantly lower than the switching frequency. As illustrated in Figure 1, the average large-signal model replaces the six switches in the power stage with three controlled voltage sources and one controlled current source, while the output stage of the power converter remains unchanged. The controlled voltage and current sources in the averaged model are defined as in (1) and (2).

$$\begin{bmatrix} \vec{v}_{AB} \\ \vec{v}_{BC} \\ \vec{v}_{CA} \end{bmatrix} = \begin{bmatrix} d_{ab} \\ d_{bc} \\ d_{ca} \end{bmatrix} \vec{v}_{dc} \quad (1)$$

$$[d_{ab}\ d_{bc}\ d_{ca}] \begin{bmatrix} \vec{\imath}_{ab} \\ \vec{\imath}_{bc} \\ \vec{\imath}_{ca} \end{bmatrix} = i_{dc} \quad (2)$$

Where $d_{ab} = (d_a - d_b), d_{bc} = (d_b - d_c), d_{ca} = (d_c - d_a)$ are the control duty cycles. Also, $\vec{\imath}_{ab} = \frac{(\vec{\imath}_a - \vec{\imath}_b)}{3}, \vec{\imath}_{bc} = \frac{(\vec{\imath}_b - \vec{\imath}_c)}{3}, \vec{\imath}_{ca} = \frac{(\vec{\imath}_c - \vec{\imath}_a)}{3}$. Where $\vec{\imath}_a, \vec{\imath}_b, \vec{\imath}_c$ are the input phase currents.

State-space equations in *abc* and *dq* coordinates in Figure 1 follow up as (3)-(6).

$$\frac{d}{dt}\begin{bmatrix} \vec{\imath}_{ab} \\ \vec{\imath}_{bc} \\ \vec{\imath}_{ca} \end{bmatrix} = \frac{1}{3L}\begin{bmatrix} \vec{v}_{AB} \\ \vec{v}_{BC} \\ \vec{v}_{CA} \end{bmatrix} - \begin{bmatrix} 0 & -\omega \\ \omega & 0 \end{bmatrix} \cdot \begin{bmatrix} \vec{\imath}_d \\ \vec{\imath}_q \end{bmatrix} - \frac{1}{3L}\begin{bmatrix} d_{ab} \\ d_{bc} \\ d_{ca} \end{bmatrix} \cdot \vec{v}_{dc} \quad (3)$$

$$\frac{d\vec{v}_{dc}}{dt} = \frac{1}{C}[d_{ab} \quad d_{bc} \quad d_{ca}] \cdot \begin{bmatrix} \vec{\imath}_{ab} \\ \vec{\imath}_{bc} \\ \vec{\imath}_{ca} \end{bmatrix} - \frac{\vec{v}_{dc}}{RC} \quad (4)$$

$$\frac{d}{dt}\begin{bmatrix} \vec{\imath}_d \\ \vec{\imath}_q \end{bmatrix} = \frac{1}{3L}\begin{bmatrix} \vec{v}_d \\ \vec{v}_q \end{bmatrix} - \begin{bmatrix} 0 & -\omega \\ \omega & 0 \end{bmatrix} \cdot \begin{bmatrix} \vec{\imath}_d \\ \vec{\imath}_q \end{bmatrix} - \frac{1}{3L}\begin{bmatrix} d_d \\ d_q \end{bmatrix} \cdot \vec{v}_{dc} \quad (5)$$

$$\frac{d\vec{v}_{dc}}{dt} = \frac{1}{C}[d_d \quad d_q] \cdot \begin{bmatrix} \vec{\imath}_d \\ \vec{\imath}_q \end{bmatrix} - \frac{\vec{v}_{dc}}{RC} \quad (6)$$

Find the steady-state operating point of the circuit in Figure 2 following as (7)-(9).

$$d_d \vec{v}_{dc} - 3\omega L \vec{\imath}_q = \vec{v}_d \quad (7)$$

$$d_q \vec{v}_{dc} - 3\omega L \vec{\imath}_d = \vec{v}_q \quad (8)$$

$$d_d \vec{\imath}_d + d_q \vec{\imath}_q = \frac{\vec{v}_{dc}}{R} \quad (9)$$

2.2. Switching circuit and control

Figure 3 illustrates the regulation of the inverter's output voltage to align with the grid voltage in terms of amplitude, phase, and frequency, achieved through feedback from the three-phase grid voltages. The inductance values of L_a, L_b, and L_c are 10 μH, with the corresponding currents and DC link voltage at the input. It is important to highlight that the DC link voltage within the feedback loop is determined after transforming the currents into the *d*-axis and *q*-axis components. The synchronous reference frame (SRF) controller utilizes Park’s transformation to regulate the inverter’s current by computing the *dq* components for the phase-locked loop (PLL) module, ensuring synchronization with the grid voltage. Consider a vector in the *abc* coordinate system, where the angles between phases *a* and *b*, *b* and *c*, and *c* and a are each 120 degrees.

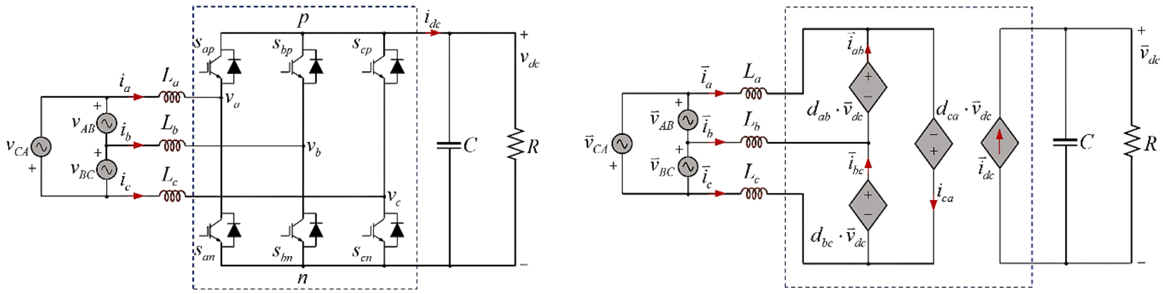

(a) (b)

Figure 1. Switching model and average model in *abc* coordinates: (a) switching model and (b) average model

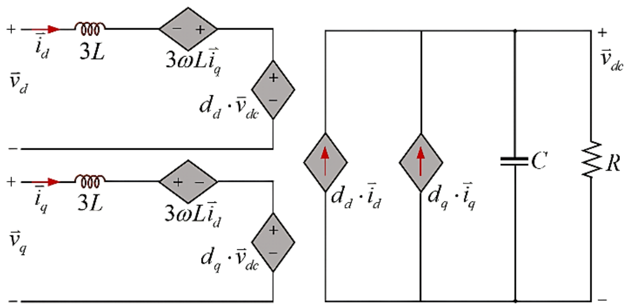

Figure 2. *dq* coordinates

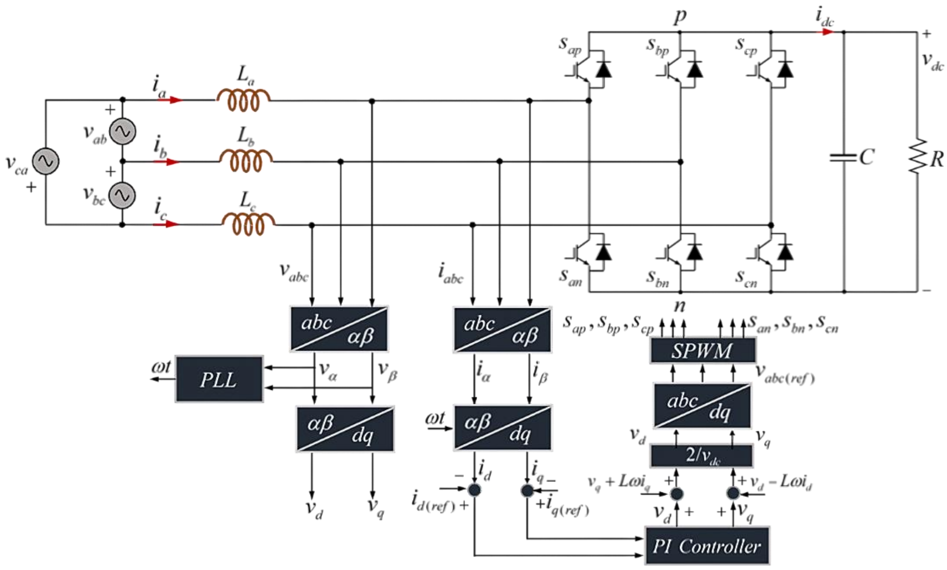

Figure 3. PI control structure for switching model

Then, from [22] and [23], the (10) is defined. The first case simulates the response of the supply during an unbalanced three-phase condition [24], [25].

$$\vec{X} = x_a \cdot \vec{a} + x_b \cdot \vec{b} + x_c \cdot \vec{c} \qquad (10)$$

Where X_x, (for $x = a, b, c$) are projections of the vector X in the directions a, b and c respectively. Also, in the $\alpha\beta$ coordinate system, we have the vector X given as (11).

$$\vec{X} = x_\alpha \cdot \vec{\alpha} + x_\beta \cdot \vec{\beta} \qquad (11)$$

Where x_α and x_β are projections of the x vector in direction of α and β, respectively. The relation between $\alpha\beta$ and abc is gotten as demonstrated below. The projection of vector x in the α-direction, x_α is given by (12) and (13).

$$x_\alpha = \vec{x} \cdot \vec{\alpha} \qquad (12)$$

$$x_\alpha = \frac{x_a - x_b}{2} - \frac{x_c}{2} \qquad (13)$$

Also, x_β projection of x vector in the direction of β is given by (14) and (15).

$$x_\beta = \vec{x} \cdot \vec{\beta} \qquad (14)$$

$$x_\beta = \frac{\sqrt{3}}{2} x_b - \frac{\sqrt{3}}{2} x_c \qquad (15)$$

Thus, as (16) and as in (17).

$$\begin{bmatrix} x_\alpha \\ x_\beta \\ 0 \end{bmatrix} = \begin{bmatrix} 1 & \frac{-1}{2} & \frac{-1}{2} \\ 0 & \frac{\sqrt{3}}{2} & -\frac{\sqrt{3}}{2} \\ \frac{1}{\sqrt{2}} & \frac{1}{\sqrt{2}} & \frac{1}{\sqrt{2}} \end{bmatrix} \begin{bmatrix} x_a \\ x_b \\ x_c \end{bmatrix} \qquad (16)$$

$$\begin{bmatrix} x_d \\ x_q \\ 0 \end{bmatrix} = \begin{bmatrix} \cos\theta & \sin\theta & 0 \\ -\sin\theta & \cos\theta & 0 \\ 0 & 0 & 1 \end{bmatrix} \begin{bmatrix} 1 & -\frac{1}{2} & -\frac{1}{2} \\ 0 & \frac{\sqrt{3}}{2} & -\frac{\sqrt{3}}{2} \\ \frac{1}{\sqrt{2}} & \frac{1}{\sqrt{2}} & \frac{1}{\sqrt{2}} \end{bmatrix} \begin{bmatrix} x_a \\ x_b \\ x_c \end{bmatrix} \qquad (17)$$

By using Clark's transformation and from $\alpha\beta$-coordinates to dq-coordinates, (18) is obtained.

$$\begin{bmatrix} x_d \\ x_q \\ 0 \end{bmatrix} = \sqrt{\frac{2}{3}} \begin{bmatrix} \cos\theta & \frac{-1}{2}\cos\theta + \frac{\sqrt{3}}{2}\sin\theta & \frac{-1}{2}\cos\theta - \frac{\sqrt{3}}{2}\sin\theta \\ -\sin\theta & \frac{1}{2}\sin\theta + \frac{\sqrt{3}}{2}\cos\theta & \frac{1}{2}\sin\theta - \frac{\sqrt{3}}{2}\cos\theta \\ \frac{1}{\sqrt{2}} & \frac{1}{\sqrt{2}} & \frac{1}{\sqrt{2}} \end{bmatrix} \qquad (18)$$

The calculation for the dq axis corresponding to the specified controller is presented in (19) and (20) [21].

$$\left[x_\alpha x_\beta\right]^T = \frac{2}{3}\left[1 \quad \frac{-1}{2} \quad \frac{-1}{2} \;;\; 0 \quad \frac{\sqrt{3}}{2} \quad -\frac{\sqrt{3}}{2}\right]^T [x_a x_b x_c]^T \qquad (19)$$

$$\left[x_d x_q\right]^T = \left[x_\alpha x_\beta\right]^T [\cos\omega t \cdot \sin\omega t - \sin\omega t \cdot \cos\omega t] \qquad (20)$$

3. RESULTS AND DISCUSSION

Boost rectifier circuit converts a 380 $V_{L\text{-}L}$ three-phase AC voltage to a 1 kV, DC voltage for electric vehicle charging applications, with parameters shown in Table 1. The parameters input resistance and DC-bus voltage are referenced from actual values in [21] and [22].

3.1. Simulation of the average model circuit

The comparison with the calculations based on (1)-(7) is presented below. The simulation results are compared with the theoretical values to assess the model's accuracy. The contribution of each equation to the analysis is discussed, along with any discrepancies that may arise.

Figure 4 shows the input power supply between voltage and current in both the *abc* and *dq* coordinates. As shown in Figures 4(a) and 4(b), the three-phase voltage waveform has a $V_{L\text{-}L}$ of 380 V and a phase shift of 30. The voltage waveform is transformed into the *dq* coordinate system, where the average voltage v_d is 658 V and v_q is 0 V. Comparing the simulation results with the calculations, v_d is 658.18 V and v_q is 0 V, which shows a high level of consistency with a discrepancy of less than 0.1%. Figures 4(c) and 4(d) show the three-phase current waveform with a value of 125 A and the current waveform transformed into the *dq* coordinates, where the average current i_d is 211.5 A and i_q is 93.5 A. Comparing the simulation results with the calculations, i_d is 151.97 A and i_q is 0 A. Discrepancy is due to the program using real values from cross-coupling, and the presence of inductance, *L*, and capacitance, *C* in the circuit, which leads to this deviation. Figure 5 shows the simulation results for the output voltage and current. Figures 5(a) and 5(b) show the DC voltage with an average value of v_{dc} is 983.054 V and the current with an average value of 98.31 A.

Table 1. Parameter

Parameter	Volume
The input phase voltage (V_{rms})	380
The power source frequency (Hz)	50
The input inductance (µH)	10
The input resistance (*Ω*)	0.1
DC-bus capacitor (µF)	100
DC-bus voltage (kV)	1
SPWM control (kHz)	20
Power charging (kW)	100
Adjustment range (%)	± 5
Charging current (A)	100
Internal resistance battery (*Ω*)	10

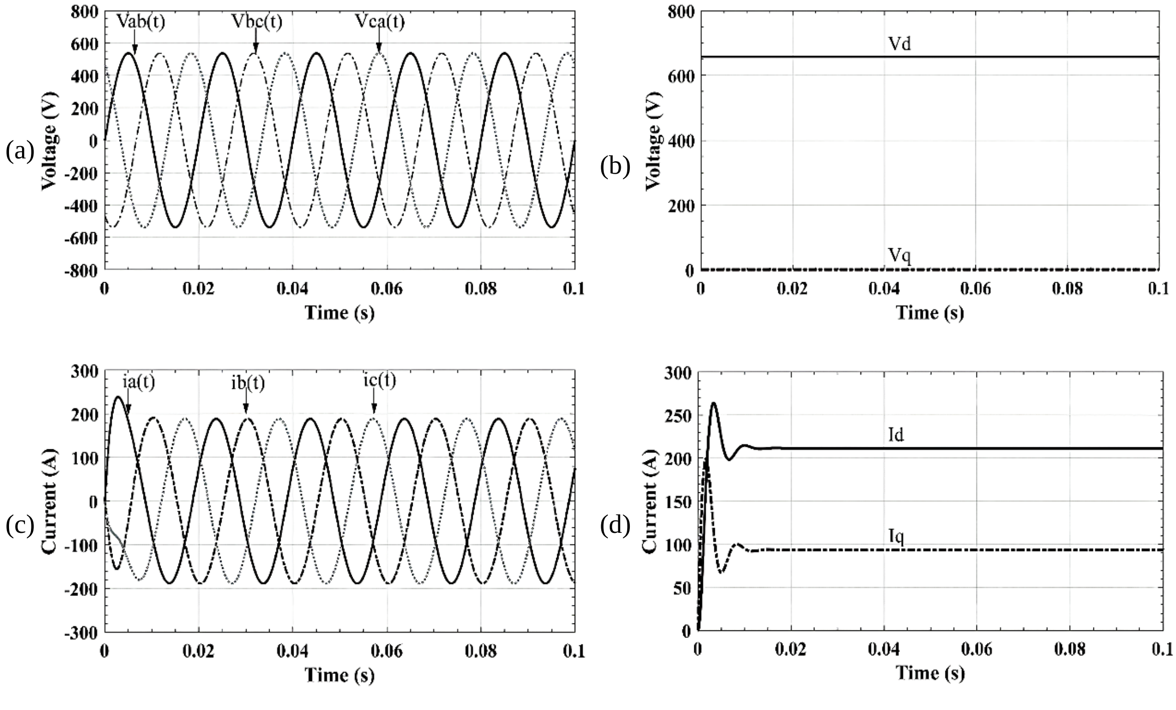

Figure 4. Input waveforms in *abc* and *dq* coordinates: (a) line-to-line voltage ($V_{L\text{-}L}$), (b) *dq-axis* voltage, (c) phase currents (i_{abc}), and (d) *dq-axis* currents

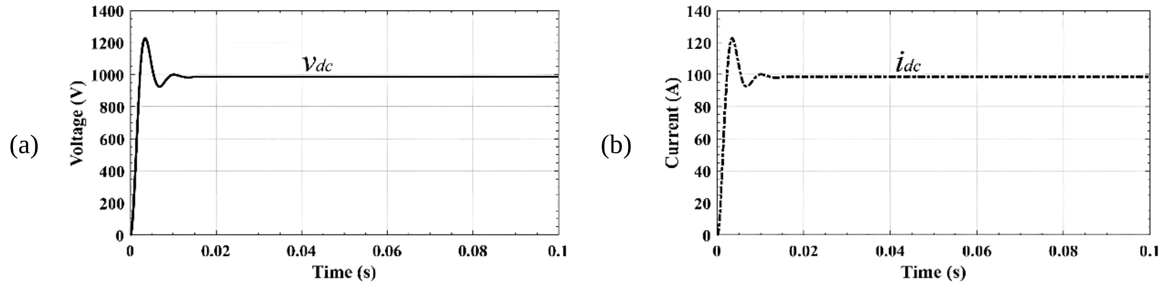

Figure 5. Output waveforms: (a) voltage (v_{dc}) and (b) current (i_{dc})

3.2. Simulation of results through switching circuit control

This section presents the simulation results through switching circuit control, covering the following cases: i) unbalanced three-phase conditions, ii) the response of a three-phase AC power supply when the voltage drops, and iii) the load step response. The details are presented as below.

3.2.1. Case 1: Unbalanced three-phase condition

The voltages are sinusoidal but unbalanced, as indicated by differing amplitudes and phase shifts between the three waveforms. This imbalance results in variations in peak values and phase shifts, deviating from an ideal balanced system. If left unaddressed, it may cause harmonic distortion, reduced efficiency, and operational issues. Figure 6 shows the simulation results for the unbalanced three-phase condition.

Figures 6(a) and 6(b) display the results of the unbalanced three-phase from 0.228 s to 0.308 s, where the voltage between phases is 380 V and the DC output voltage is 995.95 V, resulting in a ripple voltage of 18.10 V, respectively. Figures 6(c) and 6(d) show the results of the unbalanced three-phase with phase current during the time period from 0.228 s to 0.308 s, where the DC output current is 102.37 A, resulting in a ripple current of 7.25 A, respectively. From the waveform, it can be seen that the feedback control system is able to maintain stable voltage and current levels. Figure 7 shows the values of THD_v and THD_i at the input. Figures 7(a) and 7(b) display the THD values of voltage v_{ab}, which is 0.34%, and current i_a, which is 1.88%, respectively. Figures 7(c) and 7(d) show the THD values of voltage v_{bc}, which is 4.38%, and current i_b, which is 9.38%, respectively. Figures 7(e) and 7(f) show the THD values of voltage v_{ca}, which is 4.34%, and current i_c, which is 10.06%, respectively. From the data in Figures 6 and 7, it can be seen that even though there is an unbalanced three-phase condition, the system can still control and maintain stability, with THD values that are acceptable in some phases, while other phases show higher THD values, but still within a range that does not cause electrical quality issues.

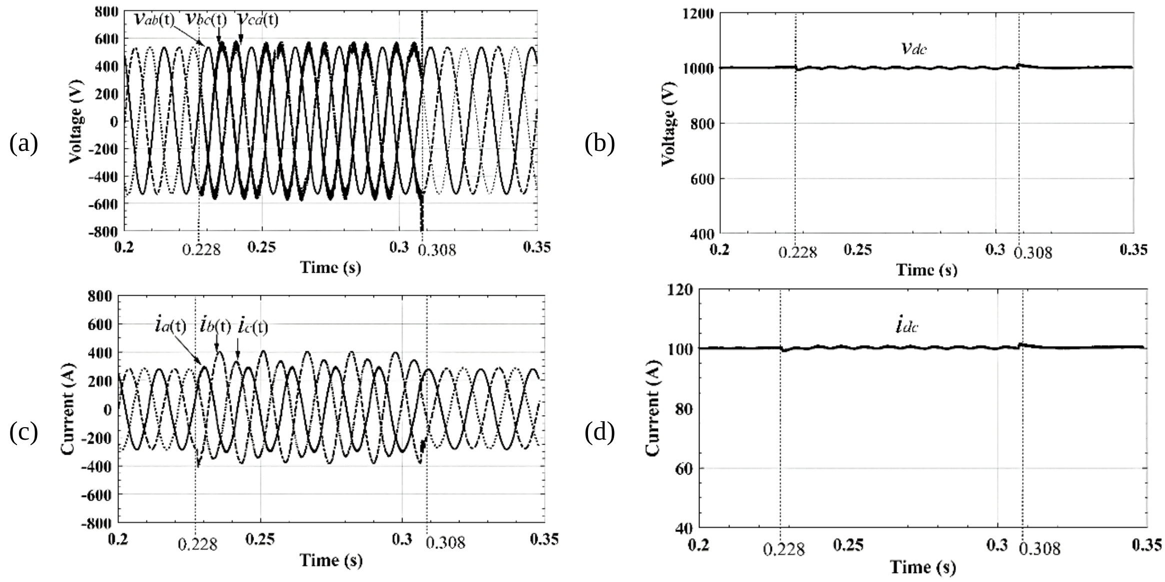

Figure 6. Waveforms under unbalanced three-phase conditions: (a) line-to-line voltage, (b) output voltage (v_{dc}), (c) input phase current (i_{abc}), and (d) output current (i_{dc})

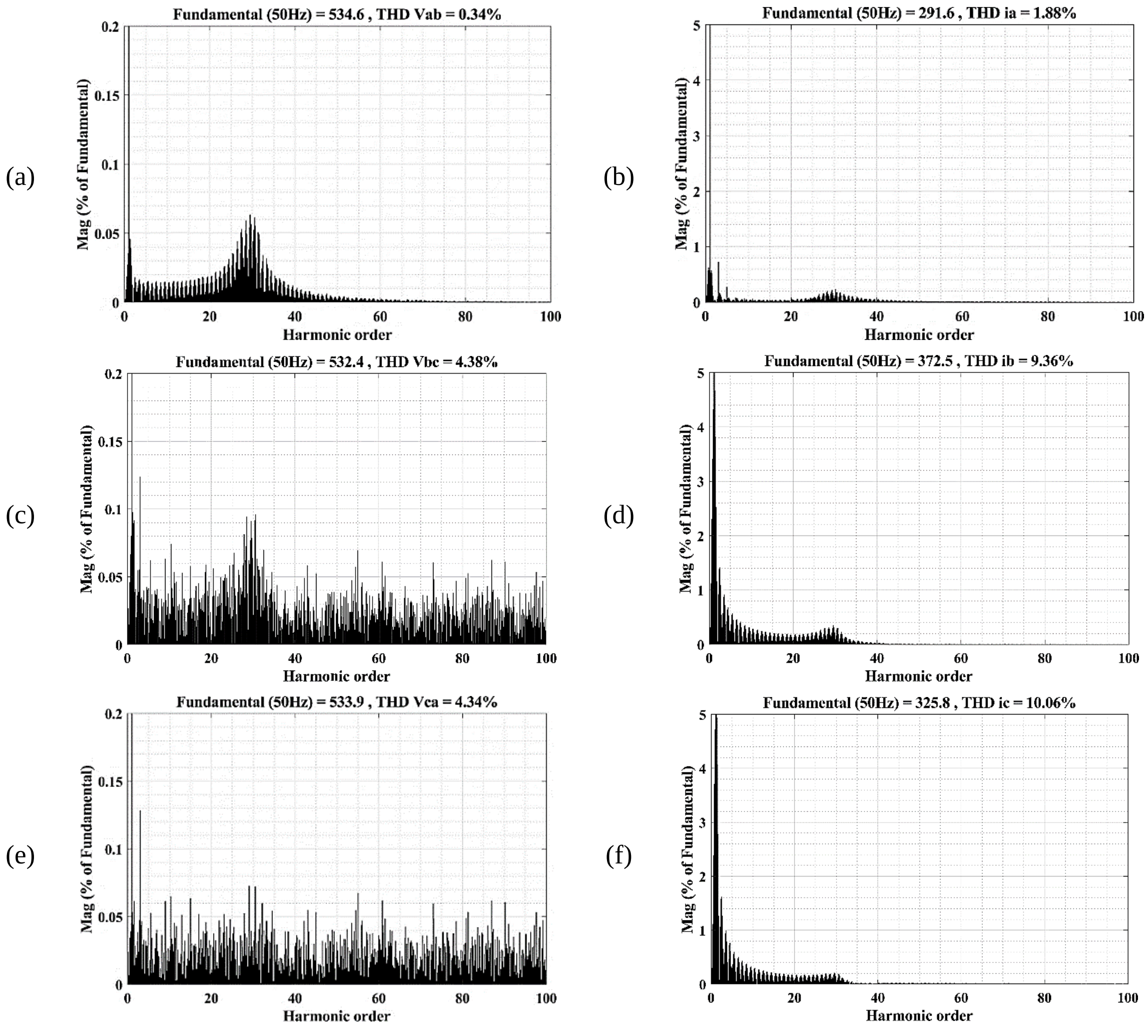

Figure 7. THD_v and THD_i results under unbalanced three-phase conditions: (a) v_{ab}, (b) i_a, (c) v_{bc}, (d) i_b, (e) v_{ca}, and (f) i_c

3.2.2. Case 2: The response of a three-phase AC power supply when the voltage drops

Simulates the response of a three-phase AC power supply when the voltage drops from its value of 100% to 80%. During the transient period, the waveforms of the voltage drop across the load and the current flowing through the load are presented. The simulation captures the dynamic behavior of the system, showing how the voltage sag affects the load, potentially causing fluctuations in the current. This transient response can lead to instability in sensitive equipment, and the effects on power quality are also observed, with potential implications for system reliability and efficiency.

Figure 8 shows the simulation results for the voltage drop condition. Figures 8(a) and 8(b) display the results of the voltage drop during the period from 0.228 s to 0.308 s, where the voltage between the 380 V line and the output DC voltage is 981.45 V, resulting in a voltage ripple of 32.55 V, respectively. Figures 8(c) and 8(d) show the results of the voltage drop for the phase current during the same period, with the output DC current being 98.10 A, resulting in a current ripple of 6.40 A, respectively. From the waveform, the feedback control system can maintain stable voltage and current levels. Figure 9 shows the values of THD for voltage and current on the input side. Figures 9(a) and 9(b) show the THD of the voltage v_{ab}, which is 6.50%, and the current i_a, which is 8.40%, respectively. Figures 9(c) and 9(d) show the THD of the voltage v_{bc}, which is 8.28%, and the current i_b, which is 8.90%, respectively. Figures 9(e) and 9(f) show the THD of the voltage v_{ca}, which is 6.47%, and the current i_c, which is 8.73%, respectively. The overall simulation results demonstrate the stability of the electrical system under conditions of voltage drop and THD. The feedback control system performs well in maintaining the stability of voltage and current even during periods of voltage reduction or high distortion. Monitoring the THD values is an important indicator for evaluating the performance of the electrical system, as a low THD value contributes to improved efficiency and reliability of the system.

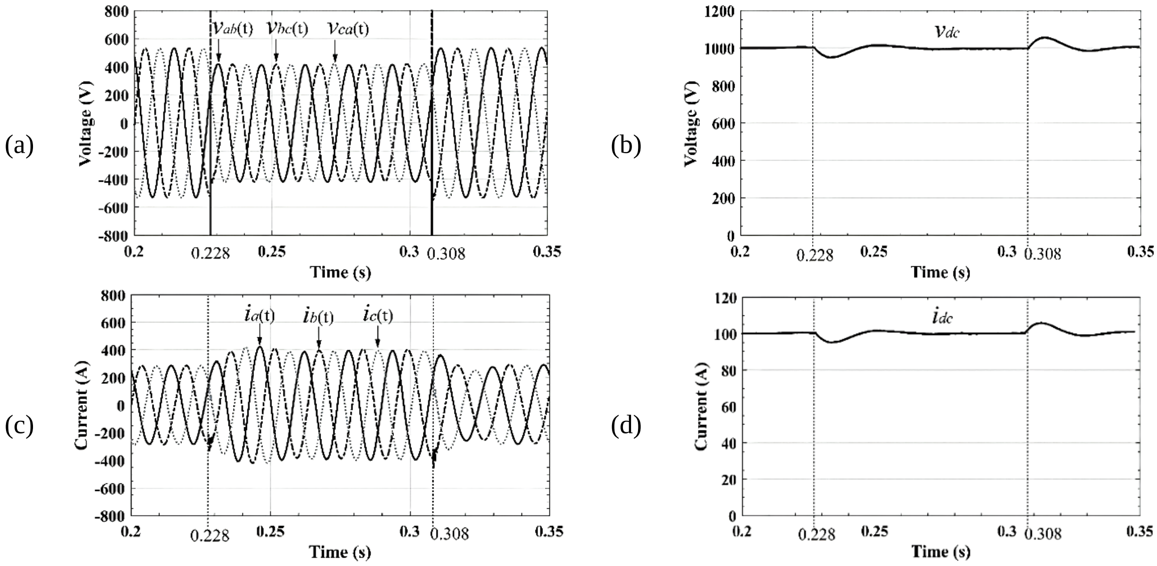

Figure 8. Response of a three-phase AC supply to voltage sags: (a) line-to-line voltage, (b) output voltage (v_{dc}), (c) input phase currents (i_{abc}), and (d) output current (i_{dc})

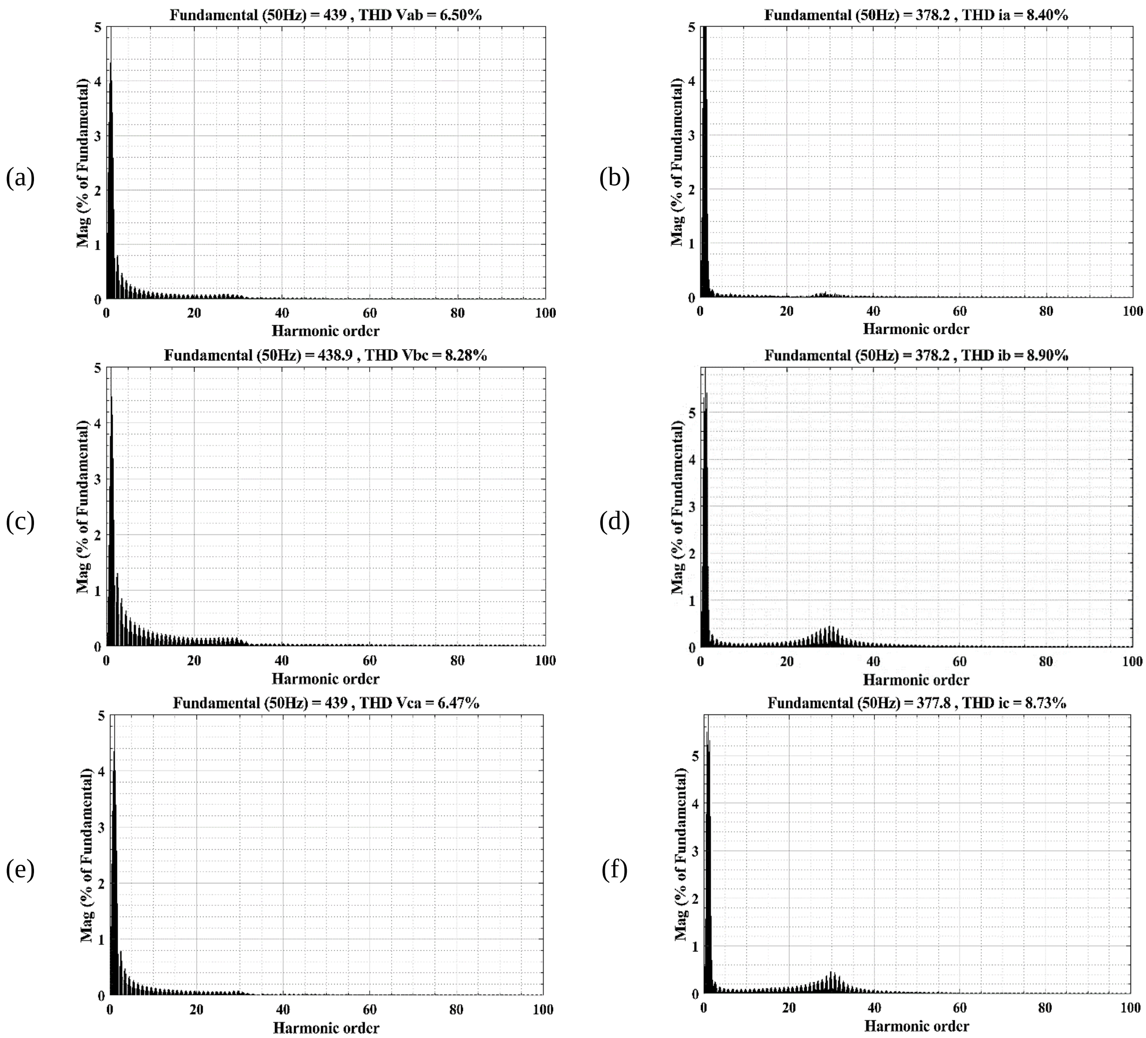

Figure 9. THD_v and THD_i results under three-phase voltage sag conditions: (a) v_{ab}, (b) i_a, (c) v_{bc}, (d) i_b, (e) v_{ca}, and (f) i_c

3.2.3. Case 3: The load step response

The simulation models the circuit's response to a sudden change in load, specifically a step response where the load decreases from 100% of its full load value to just 10%. This simulation focuses on capturing the transient behavior that occurs when the load is abruptly reduced, resulting in an immediate shift in the system's operating conditions. As the load decreases, the voltage and current waveforms adjust in real-time to meet the new load demand. This scenario is particularly useful for assessing the system's ability to recover and stabilize after such a drastic reduction in load. The simulation records key dynamic parameters, such as overshoot, settling, and any fluctuations in the output that may occur as the system compensates for the load change. These metrics are critical for evaluating the system's performance during transient events. Additionally, the impact on system performance is thoroughly analyzed, with a focus on aspects like changes in efficiency, power quality, and the potential for voltage or current spikes during the transition. This helps identify potential risks to the system's stability, such as power quality degradation, overvoltage, or overcurrent conditions that may arise from the load change. The analysis of these factors provides valuable insights into how well the system can maintain reliable operation under sudden load variations and helps assess the overall stability and robustness of the system.

Figure 10 shows the simulation results for the load step response condition. In Figures 10(a) and 10(b), the load step response is depicted during the period from 0.228 s to 0.308 s, where the voltage between the 380 V line and the v_{dc} is 993.75 V, resulting in a ripple voltage of 22.50 V. These figures clearly illustrate the voltage adjustment as the load changes and the transient behavior that occurs due to the sudden load reduction. The voltage ripple seen here is an indication of the system's response to the load step, showing how the system compensates for the load change and stabilizes over time. In Figures 10(c) and 10(d), the load step response for the current in each phase is shown during the same period. The i_{dc} is measured at 109.30 A, resulting in a ripple current of 1.20 A. These figures demonstrate how the current waveform fluctuates as the load step occurs, with the current ripple indicating transient effects as the system adjusts to the new load condition. The current waveforms highlight the system's ability to manage the load step and stabilize the output, ensuring that the current levels eventually settle within acceptable limits. The observed voltage and current ripples are crucial for understanding the transient performance of the system and the effectiveness of the control mechanisms in place. These results also provide insights into the potential impacts on power quality, as fluctuations in voltage and current could influence the overall performance and stability of sensitive equipment connected to the system.

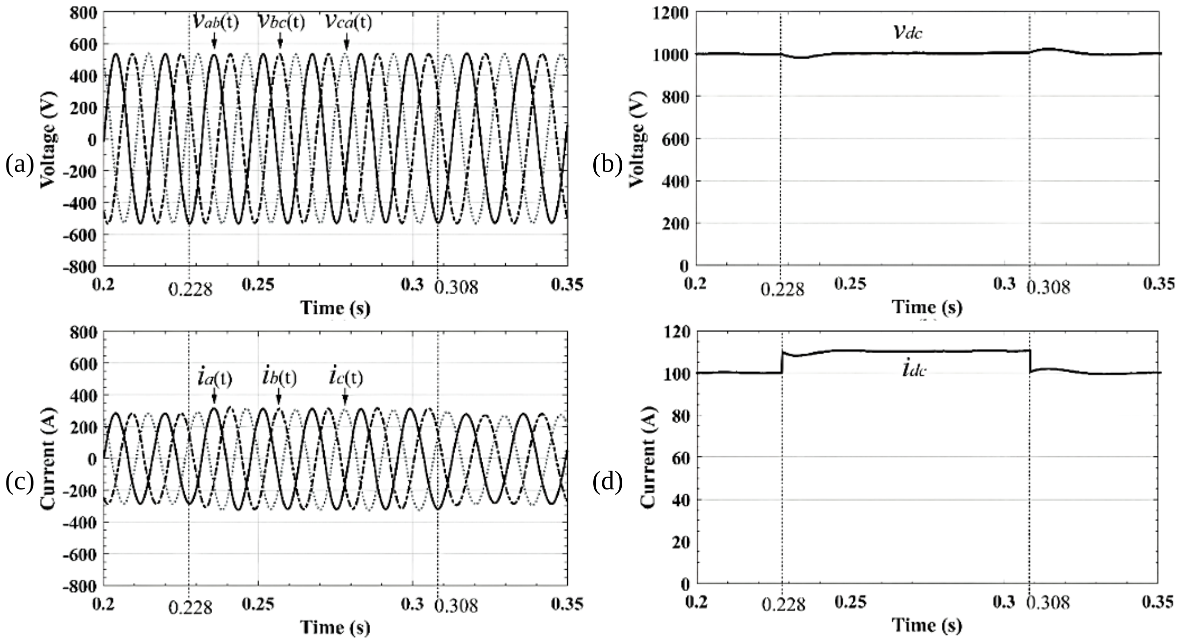

Figure 10. Load step response: (a) line-to-line voltage, (b) output voltage (v_{dc}), (c) input phase currents (i_{abc}), and (d) output current (i_{dc})

Figure 11 shows the THD of voltage and current at the input. In Figures 11(a) and 11(b), the THD values for the voltage v_{ab} are 0.06%, and for the current i_a, it is 2.85%, respectively. Figures 11(c) and 11(d) show the THD values for the voltage v_{bc}, which is 0.06%, and the current i_b, which is 2.91%, respectively. Figures 11(e) and 11(f) show the THD values for the voltage v_{ca}, which is 0.06%, and the current i_c, which is 2.85%, respectively. The ripple values for both voltage and current during the specified time period may reflect imperfect changes in the system, but overall, the results from the simulation are considered acceptable, especially when compared to the low THD values for the measured voltage and current.

From Table 2, when the system is in unbalanced three-phase conditions, it can be observed that the THD of voltage and current is significantly distorted, especially in the currents of phases *b* and *c*. This demonstrates the impact of system imbalance, which leads to increased harmonic distortion. The voltage drop causes a clear increase in the THD values of both voltage and current, indicating the inadequacy of the voltage supply that may affect the system's performance. The load response shows the least distortion in both voltage and current, which may be due to the continuously changing load that helps the system maintain better stability.

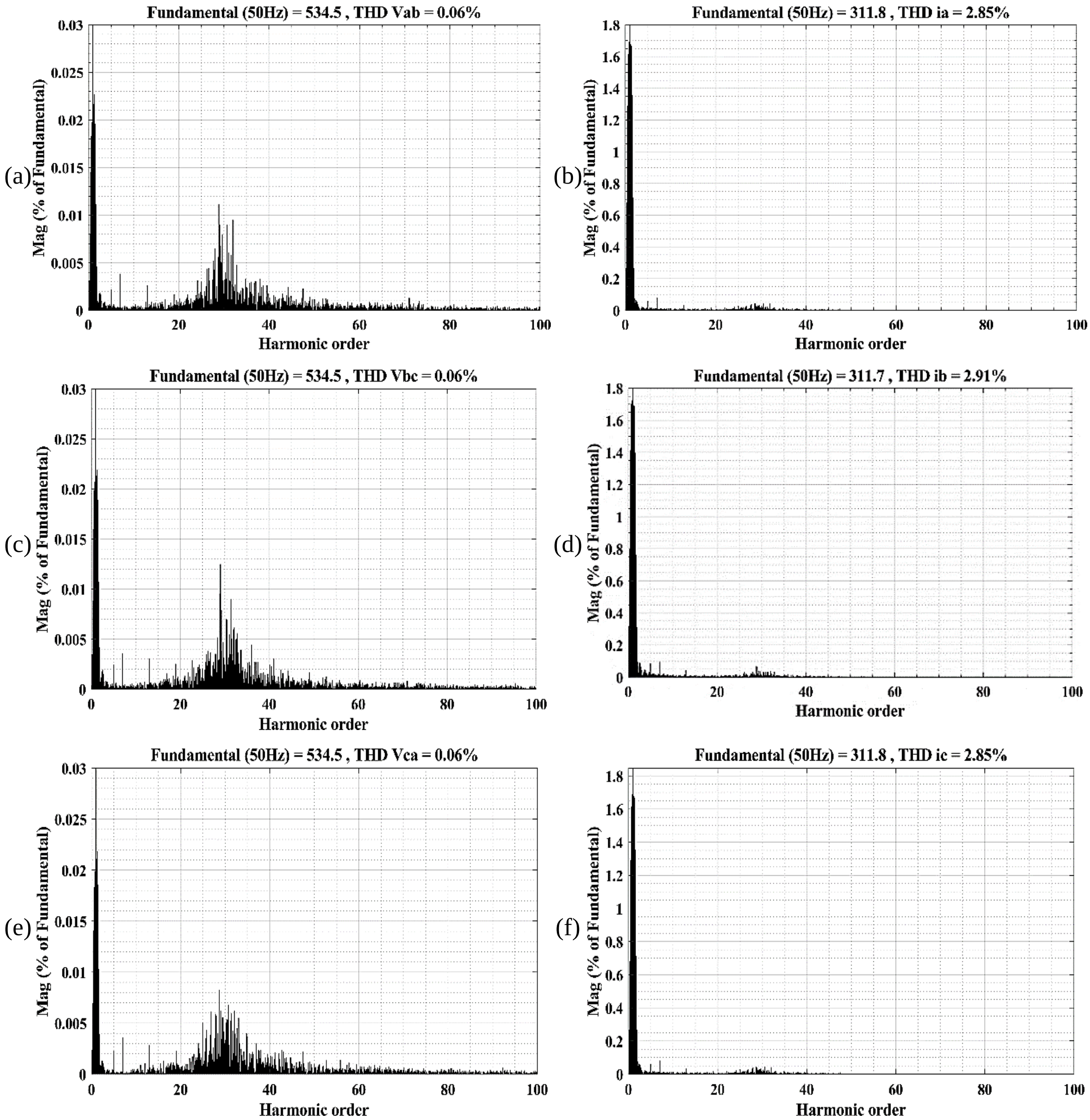

Figure 11. THD_v and THD_i results during load step response: (a) v_{ab}, (b) i_a, (c) v_{bc}, (d) i_b, (e) v_{ca}, and (f) i_c

Table 2. Compare the properties of each case

Parameter	Unbalanced three-phase condition	Voltage drop	Load step response
v_{dc} (V)	995.95	981.45	993.75
v_{ripple} (V)	18.10	32.55	22.50
i_{dc} (A)	102.37	98.10	109.30
i_{ripple} (A)	7.25	6.40	1.20
THDv_{ab} (%)	0.34	6.50	0.06
THDv_{bc} (%)	4.38	8.28	0.06
THDv_{ca} (%)	4.34	6.47	0.06
THDi_a (%)	1.88	8.40	2.85
THDi_b (%)	9.36	8.90	2.91
THDi_c (%)	10.06	8.73	2.85

4. CONCLUSION

The analysis of system performance in both the *abc* and *dq* coordinate systems demonstrates a high level of consistency between the simulation and theoretical calculations. The average *dq* frame voltage was found to be 658 V for v_d and 0 V for v_q, with a discrepancy of less than 0.1% from the calculated values, indicating accurate voltage transformation between reference frames. For the *dq* frame currents, the simulation results showed i_d at 211.50 A and i_q at 93.50 A, while the calculated values were 151.97 A for I_d and 0 A for I_q. The deviation is primarily attributed to cross-coupling effects between the *d* and *q* axes, as well as the influence of inductive and capacitive elements within the circuit. These factors introduce dynamic interactions that are not fully captured in idealized theoretical models but are evident in the simulation. The output DC voltage and current were found to be 983.054 V and 98.31 A, respectively, demonstrating stable operation under nominal conditions. Further analysis of system behavior under three different scenarios unbalanced three-phase operation, voltage drop, and load step response revealed variations in total harmonic distortion (THD). The unbalanced condition exhibited the highest THD for both voltage and current due to phase asymmetry, while the voltage drop scenario further increased THD, highlighting the system's sensitivity to sudden reductions in supply voltage. Conversely, the load step response resulted in the lowest THD, indicating the system's ability to maintain stable operation under dynamic load changes. Overall, the system exhibited minimal deviation from theoretical predictions and maintained stable voltage and current across different operating conditions. The findings highlight the importance of incorporating cross-coupling effects and circuit reactance into analytical models to improve prediction accuracy. Additionally, the results confirm the system's robustness in handling various operational disturbances while maintaining acceptable performance levels.

FUNDING INFORMATION

The authors would like to express their appreciation for the financial support and research facilities provided by the Faculty of Industry and Technology, Rajamangala University of Technology Isan, Thailand, through the Flagship RMUTI Grant No. FF66-P6-001 in 2023.

AUTHOR CONTRIBUTIONS STATEMENT

This journal uses the Contributor Roles Taxonomy (CRediT) to recognize individual author contributions, reduce authorship disputes, and facilitate collaboration.

Name of Author	C	M	So	Va	Fo	I	R	D	O	E	Vi	Su	P	Fu
Jeerapong Srivichai	✓	✓	✓	✓	✓	✓		✓	✓	✓			✓	
Kittaya Somsai		✓			✓	✓	✓	✓	✓		✓	✓		
Nithiroth Pornsuwancharoen	✓		✓	✓	✓	✓			✓	✓	✓		✓	

C : **C**onceptualization
M : **M**ethodology
So : **So**ftware
Va : **Va**lidation
Fo : **Fo**rmal analysis
I : **I**nvestigation
R : **R**esources
D : **D**ata Curation
O : Writing - **O**riginal Draft
E : Writing - Review & **E**diting
Vi : **Vi**sualization
Su : **Su**pervision
P : **P**roject administration
Fu : **Fu**nding acquisition

CONFLICT OF INTEREST STATEMENT

The authors declare that they have no known competing financial interests or personal relationships that could have appeared to influence the work reported in this paper.

DATA AVAILABILITY

Data availability is not applicable to this paper as no new data were created or analyzed in this study.

REFERENCES

[1] G. Rajendran, C. A. Vaithilingam, K. Naidu, and K. S. P. Oruganti, "Energy-efficient converters for electric vehicle charging stations," *SN Applied Sciences*, vol. 2, no. 4, 2020, doi: 10.1007/s42452-020-2369-0.

[2] S. Chakraborty, H. N. Vu, M. M. Hasan, D. D. Tran, M. El Baghdadi, and O. Hegazy, "DC-DC converter topologies for electric vehicles, plug-in hybrid electric vehicles and fast charging stations: State of the art and future trends," *Energies*, vol. 12, no. 8, 2019, doi: 10.3390/en12081569.

[3] G. Town, S. Taghizadeh, and S. Deilami, "Review of fast charging for electrified transport: demand, technology, systems, and planning," *Energies*, vol. 15, no. 4, p. 1276, Feb. 2022, doi: 10.3390/en15041276.

[4] A. Stanojevic, Y. E. Bouvier, and P. J. Grbovic, "Comparison of 2-stage isolated converters for fast EV charger, using partial power," in *IECON 2022–48th Annual Conference of the IEEE Industrial Electronics Society*, 2022, doi: 10.1109/IECON49645.2022.9968597.

[5] S. Kodeeswaran, M. Nandhini Gayathri, P. Sanjeevikumar, and R. Peña-Alzola, "High-power converters and challenges in electric vehicle wireless charging – a review," *IETE Journal of Research*, vol. 70, no. 3, pp. 3167–3186, Mar. 2024, doi: 10.1080/03772063.2023.2186958.

[6] S. Palanisamy, S. Chenniappan, and S. Padmanaban, "Fast-charging infrastructure for electric vehicles," in *Fast-Charging Infrastructure for Electric and Hybrid Electric Vehicles*, Wiley, 2023, pp. 181–188, doi: 10.1002/9781119987772.ch11.

[7] S. Palanisamy, S. Chenniappan, and S. Padmanaban, "Batteries for fast-charging infrastructure," in *Fast-Charging Infrastructure for Electric and Hybrid Electric Vehicles*, Wiley, 2023, pp. 51–58, doi: 10.1002/9781119987772.ch4.

[8] S. Palanisamy, S. Chenniappan, and S. Padmanaban, "Selection of fast-charging station," in *Fast-Charging Infrastructure for Electric and Hybrid Electric Vehicles*, Wiley, 2023, pp. 31–38, doi: 10.1002/9781119987772.ch2.

[9] S. Mateen, M. Amir, A. Haque, and F. I. Bakhsh, "Ultra-fast charging of electric vehicles: A review of power electronics converter, grid stability and optimal battery consideration in multi-energy systems," *Sustainable Energy, Grids and Networks*, vol. 35, p. 101112, Sep. 2023, doi: 10.1016/j.segan.2023.101112.

[10] L. Wang, Z. Qin, T. Slangen, P. Bauer, and T. Van Wijk, "Grid impact of electric vehicle fast charging stations: trends, standards, issues and mitigation measures - an overview," *IEEE Open Journal of Power Electronics*, vol. 2, pp. 56–74, 2021, doi: 10.1109/OJPEL.2021.3054601.

[11] G. Arena, A. Chub, M. Lukianov, R. Strzelecki, D. Vinnikov, and G. De Carne, "A comprehensive review on DC fast charging stations for electric vehicles: Standards, power conversion technologies, architectures, energy management, and cybersecurity," *IEEE Open Journal of Power Electronics*, 2024, doi: 10.1109/OJPEL.2024.3466936.

[12] C. Cataldo-Díaz, R. Linfati, and J. W. Escobar, "Mathematical models for the electric vehicle routing problem with time windows considering different aspects of the charging process," *Operational Research*, vol. 24, no. 1, Mar. 2024, doi: 10.1007/s12351-023-00806-5.

[13] M. Diab Hraiz and J. A. M. García, "Harmonics emissions and power system grid resilience in electric vehicle charging," in *Power Quality - New Insights [Working Title]*, IntechOpen, 2024, doi: 10.5772/intechopen.1004261.

[14] P. Sharma, D. K. Palwalia, A. K. Sharma, N. Priyadarshi, and S. Padmanaban, "Coati optimized FOPID controller for non-isolated DC–DC converters in EV charging application," *IET Power Electronics*, vol. 17, no. 16, pp. 2771–2784, Dec. 2024, doi: 10.1049/pel2.12798.

[15] H. Tian, D. Tzelepis, and P. N. Papadopoulos, "Electric vehicle charger static and dynamic modeling for power system studies," *Energies*, vol. 14, no. 7, p. 1801, Mar. 2021, doi: 10.3390/en14071801.

[16] H. Polat *et al.*, "A review of DC fast chargers with BESS for electric vehicles: Topology, battery, reliability oriented control and cooling perspectives," *Batteries*, vol. 9, no. 2, p. 121, 2023, doi: 10.3390/batteries9020121.

[17] D. P. Stojanović, L. M. Korunović, and J. V. Milanović, "Dynamic load modelling based on measurements in medium voltage distribution network," *Electric Power Systems Research*, vol. 78, no. 2, pp. 228–238, Feb. 2008, doi: 10.1016/j.epsr.2007.02.003.

[18] S. Deb, K. Tammi, K. Kalita, and P. Mahanta, "Impact of electric vehicle charging station load on distribution network," *Energies*, vol. 11, no. 1, p. 178, Jan. 2018, doi: 10.3390/en11010178.

[19] A. Simarro-garcía, R. Villena-ruiz, A. Honrubia-escribano, M. Abdou-tankari, E. Gómez-lázaro, and G. Lefebvre, "Fast and extreme fast charging integration for electric vehicles: impact on an industrial distribution network," *International Journal of Engineering Science and Application*, vol. 8, no. 2, pp. 58–64, 2024, [Online]. Available: https://dergipark.org.tr/en/pub/ijesa/issue/85715/1353721

[20] P. Aree and W. Nakawiro, "Electrical modeling and simulation of industrial power system with MATLAB/Simulink program," in *Power and Energy Systems*, Calgary, AB, Canada: ACTAPRESS, 2013, pp. 347–352, doi: 10.2316/P.2013.800-054.

[21] L. Wang, *PID Control System Design and Automatic Tuning using MATLAB/Simulink*. John Wiley & Sons, 2020, doi: 10.1002/9781119469414.

[22] H. Tian, D. Tzelepis, and P. N. Papadopoulos, "Electric vehicle charger static and dynamic modeling for power system studies," *Energies*, vol. 14, no. 7, p. 1801, Mar. 2021, doi: 10.3390/en14071801.

[23] S. Bogimi, "A grid interconnected nested neutral-point clamped inverter with voltage synchronization using synchronous reference frame controller," *International Journal of Applied Power Engineering (IJAPE)*, vol. 10, no. 4, p. 364, Dec. 2021, doi: 10.11591/ijape.v10.i4.pp364-372.

[24] A. Dandoussou and P. Kenfack, "Modelling and analysis of three-phase grid-tied photovoltaic systems," *Journal of Electrical Systems and Information Technology*, vol. 10, no. 1, p. 26, May 2023, doi: 10.1186/s43067-023-00096-z.

[25] M. Restrepo, J. Morris, M. Kazerani, and C. A. Cañizares, “Modeling and testing of a bidirectional smart charger for distribution system EV integration,” *IEEE Transactions on Smart Grid*, vol. 9, no. 1, pp. 152–162, 2016, doi: 10.1109/TSG.2016.2547178.

BIOGRAPHIES OF AUTHORS

Jeerapong Srivichai received the B.Eng. degree in Electrical Engineering from Pathumwan Institute of Technology, Bangkok, Thailand, in 2003 and M.Eng. degree in Electrical Engineering from Kasetsart University, Bangkok, Thailand, in 2008, and Ph.D. degree in Electric Engineering from Suranaree University of Technology, Nakhon Ratchasima, Thailand, in 2020. Currently, he is an assistant professor at the Department of Electrical Engineering, Rajamangala University of Technology Isan Sakon Nakhon Campus. His research interests include railway electrification, electric vehicles, power electronics, and induction heating. He can be contacted at email: geerapong.sr@rmuti.ac.th.

Kittaya Somsai is currently an assistant professor in the Department of Electrical Engineering, Rajamangala University of Technology Isan Sakon Nakhon Campus, Thailand. He received the B.Eng. in Electrical Engineering from Rajamangala's Institute of Technology, Thailand in 2003 and M.Eng. degree in Electrical Engineering from King Mongkut's Institute of Technology North Bangkok, Thailand in 2005, and Ph.D. in Electrical Engineering from Suranaree University of Technology, Thailand, in 2012. His research interests are in power systems, custom power devices, power electronics and control, and artificial intelligence techniques. He can be contacted at email: kittaya.so@rmuti.ac.th.

Nithiroth Pornsuwancharoen received the B.S.Tech.Ed., M.S.Tech.Ed., and Ph.D. degrees in Telecommunication Engineering and Applied Physics from the King Mongkut’s Institute of Technology Ladkrabang, Bangkok, Thailand, in 1998, 2005, and 2009, respectively. He is a lecturer with the Department of Electrical Engineering, Faculty of Industry and Technology, Rajamangala University of Technology Isan Sakon Nakhon Campus, Sakon Nakhon, Thailand. His current research interests are fast-charging, circuits, micro-ring resonator, soliton communication, IoT, and quantum communication. He can be contacted at email: nithiroth.po@rmuti.ac.th.